

Response optimization of a three-axis sensitive SERF magnetometer for closed-loop operation

Yuanrui Zhou(周原锐), Yongze Sun(孙永泽), Xixi Wang(汪茜茜), Jianan Qin(秦佳男), Xue Zhang(张雪), and Yanzhang Wang(王言章)

Citation: Chin. Phys. B, 2024, 33 (**2**): 020701. DOI: 10.1088/1674-1056/ad0b00
Journal homepage: http://cpb.iphy.ac.cn; http://iopscience.iop.org/cpb

What follows is a list of articles you may be interested in

A compact and closed-loop spin-exchange relaxation-free atomic magnetometer for wearable magnetoencephalography

Qing-Qian Guo(郭清乾), Tao Hu(胡涛), Xiao-Yu Feng(冯晓宇), Ming-Kang Zhang(张明康), Chun-Qiao Chen(陈春巧), Xin Zhang(张欣), Ze-Kun Yao(姚泽坤), Jia-Yu Xu(徐佳玉),Qing Wang(王青), Fang-Yue Fu(付方跃), Yin Zhang(张寅), Yan Chang(常严), and Xiao-Dong Yang(杨晓冬)
Chin. Phys. B, 2023, 32 (**4**): 040702. DOI: 10.1088/1674-1056/ac7e38

Dynamic range and linearity improvement for zero-field single-beam atomic magnetometer

Kai-Feng Yin(尹凯峰), Ji-Xi Lu(陆吉玺), Fei Lu(逯斐), Bo Li(李博), Bin-Quan Zhou(周斌权), and Mao Ye(叶茂)
Chin. Phys. B, 2022, 31 (**11**): 110703. DOI: 10.1088/1674-1056/ac6010

Magnetic shielding property for cylinder with circular, square, and equilateral triangle holes

Si-Yuan Hao(郝思源), Xiao-Ping Lou(娄小平), Jing Zhu(祝静), Guang-Wei Chen(陈广伟), and Hui-Yu Li(李慧宇)
Chin. Phys. B, 2021, 30 (**6**): 060702. DOI: 10.1088/1674-1056/abeeee

A modified analytical model of the alkali-metal atomic magnetometer employing longitudinal carrier field

Chang Chen(陈畅), Yi Zhang(张燚), Zhi-Guo Wang(汪之国), Qi-Yuan Jiang(江奇渊), Hui Luo(罗晖), and Kai-Yong Yang(杨开勇)
Chin. Phys. B, 2021, 30 (**5**): 050707. DOI: 10.1088/1674-1056/abd7d3

Search for topological defect of axionlike model with cesium atomic comagnetometer

Yucheng Yang(杨雨成), Teng Wu(吴腾), Jianwei Zhang(张建玮), and Hong Guo(郭弘)
Chin. Phys. B, 2021, 30 (**5**): 050704. DOI: 10.1088/1674-1056/abf132

Response optimization of a three-axis sensitive SERF magnetometer for closed-loop operation

Yuanrui Zhou(周原锐)[1,2], Yongze Sun(孙永泽)[1,2], Xixi Wang(汪茜茜)[1,2], Jianan Qin(秦佳男)[1,2], Xue Zhang(张雪)[3,4], and Yanzhang Wang(王言章)[1,2,†]

[1] *Key Laboratory of Geophysical Exploration Equipment (Ministry of Education), Jilin University, Changchun* 130012, *China*
[2] *College of Instrumentation and Electrical Engineering, Jilin University, Changchun* 130012, *China*
[3] *Department of Physics, Johannes Gutenberg-Universitat Mainz*, 55128 *Mainz, Germany*
[4] *Helmholtz-Institut, GSI Helmholtzzentrum fur Schwerioneforschung*, 55128 *Mainz, Germany*

(Received 27 June 2023; revised manuscript received 29 October 2023; accepted manuscript online 9 November 2023)

Most triaxial-vectorial magnetic field measurements with spin-exchange relaxation free (SERF) atomic magnetometer (AM) are based on the quasi-steady-state solution of the Bloch equation. However, the responding speed of these methods is greatly limited because the frequency of the modulation signal should be slow enough to ensure the validity of the quasi-steady-state solution. In this work, a new model to describe the response of the three-axis sensitive SERF AM with high modulation frequency is presented and verified. The response of alkali-atomic spin to high-frequency modulation field is further investigated by solving the Bloch equation in a modulation-frequency-dependence manner. This solution is well verified by our experiments and can offer a reference for selection of modulation frequencies. The result shows a potential to achieve a SERF AM operating in a geomagnetic field without heavy aluminum shielding when the modulation frequencies are selected properly.

Keywords: triaxial-vectorial magnetic field measurement, spin-exchange relaxation free, atomic magnetometer

PACS: 07.55.–w, 07.55.Ge, 85.70.Sq **DOI:** 10.1088/1674-1056/ad0b00

1. Introduction

Ultrahigh-sensitive atomic magnetometers (AMs) have been used in many applications, from searches for physics beyond the standard model, magnetic resonance imaging to magnetoencephalography (MEG), magnetocardiography (MCG), and so on.[1–6] Currently, the most sensitive AM is the spin-exchange relaxation free (SERF) magnetometer.[7] With sensitivities comparable to the traditional superconducting quantum interference devices (SQUIDs) operating at cryogenic temperature, SERF magnetometers also offer other advantages such as low-power dissipation, compact packaging, and the absence of complex cryogenic equipment.

Most commonly, AMs monitor the precession frequency of the atomic spin polarization to measure the magnetic field, which leads to a scalar operation mode.[8] The detection of the magnitude of the spin polarization projection makes it possible for the SERF AM to be sensitive to the vector fields. However, in most configurations, no matter whether the traditional orthogonal pump-probe configuration,[9–11] parallel pump-probe configuration,[12,13] or single beam configuration is adopted,[14,15] the SERF AM just acts as a single-axis sensor. For some applications, however, trixial magnetic vectors are also important such as geophysics and MEG. To this end, various kinds of precession modulation methods were applied to the atomic system to demodulate the magnetic vectors.

In 2004, Seltzer *et al.* designed an unshielded three-axis SERF AM achieving a sensitivity on an order of 1 pT/$\sqrt{\text{Hz}}$ by modulating two AC magnetic fields at different frequencies in the directions of the pumping beam and the vertical probing beam respectively.[16] In 2006, Li *et al.* modulated a large magnetic field in the direction of the pumping axis, constructing a two-axis AM capable of detecting transverse magnetic field with a white noise level of 60 fT/$\sqrt{\text{Hz}}$.[17] In 2015, by utilizing two additional light-shift beams for modulation, Patton *et al.* constructed a full-light vector magnetometer that could measure the direction of transverse field with a noise of 0.5 mrad/$\sqrt{\text{Hz}}$.[18] In the same year, Huang *et al.* demonstrated a triaxial magnetic field detection method, based on a Bell–Bloom magnetometer, which applied a pulsed pumping beam resonating with the magnetic field. Sensitivities of 0.8 pT/$\sqrt{\text{Hz}}$ in x axis and 1.5 pT/$\sqrt{\text{Hz}}$ in y and z axes were achieved.[19] After that, by rotating field in the x–y plane and modulating another field in the z axis, they designed a single-beam three-axis AM in 2016, obtained sensitivities of 300 fT/$\sqrt{\text{Hz}}$ in x and y axes and 3 pT /$\sqrt{\text{Hz}}$ in z axis.[20]

Due to the SERF regime's requirements for low Larmor frequencies, the methods with capability of obtaining the value of the three-axis magnetic field simultaneously and canceling the magnetic field to zero by feedback are very suitable for the triaxial-vectorial magnetic field detection of the SERF AM, such as the work of Seltzer and Romalis[16] and Huang *et al.*[20] Benefiting from the feedback, these ap-

†Corresponding author. E-mail: yanzhang@jlu.edu.cn
© 2024 Chinese Physical Society and IOP Publishing Ltd

proaches may also extend the application scenarios of SERF AMs to geomagnetic field environments, as has been achieved in Ref. [16]. In this kind of method, the magnetic fields of different frequencies are modulated on each axis, and the offset fields of the respective axes are demodulated from the output signals. However, the current demodulation process is usually based on the steady-state solution of the Bloch equation, which causes the frequency modulation that must be slow enough to valid the quasi-steady-state solution. As a result, the bandwidth of the system is greatly limited. This disadvantage is even more unacceptable when we wish to utilize this method with active magnetic field cancelation to operate SERF magnetometers in a non-magnetic shielding environment because of the power line noise. This is also the reason why Seltzer used a heavy aluminum shielding in his work.[16]

In this work, the response of a three-axis sensitive SERF magnetometer designed based on Seltzer's steady-state solution method is further investigated, especially with higher modulation frequencies beyond the steady-state solution. A theory is presented to explain the response of the system to high frequency modulation fields, which will offer a reference for selection of the modulation frequency. The magnetic field canceling experiment based on the theory shows a potential to operate the SERF AM under a geomagnetic field environment without heavy aluminum shielding.

2. Experimental setup

The schematic of the experimental setup is shown in Fig. 1. A potassium based two-optical-axial SERF magnetometer is placed in a cylinder magnetic shield consisting of four-layer μ-metal (Twinleaf, MS-2). The potassium vapor cell is heated to 180°C with an oven driven by high-frequency AC current of 100 kHz. Two commercial distributed feedback (DFB) lasers are used for pumping and probing. Both the beams are fiber coupled into the shielding and collimated. The pumping beam propagating along $\hat{z}$ axis is circularly polarized by a linear polarizer and a quarter-wave plate, and the wavelength is tuned to the D1 resonance of potassium at 770.106 nm. The prob beam propagating along $\hat{x}$ axis is linearly polarized and is detuned to 770.013 nm. The potassium atoms are spin polarized by the pumping beam, and the $\hat{x}$ component of spin polarization P_x is measured with the optical rotation of the probing beam. After the probing beam passes through the cell, this optical rotation is analyzed by a polarimeter consisting of a polarization beam splitter (PBS) and a balanced photodetector.

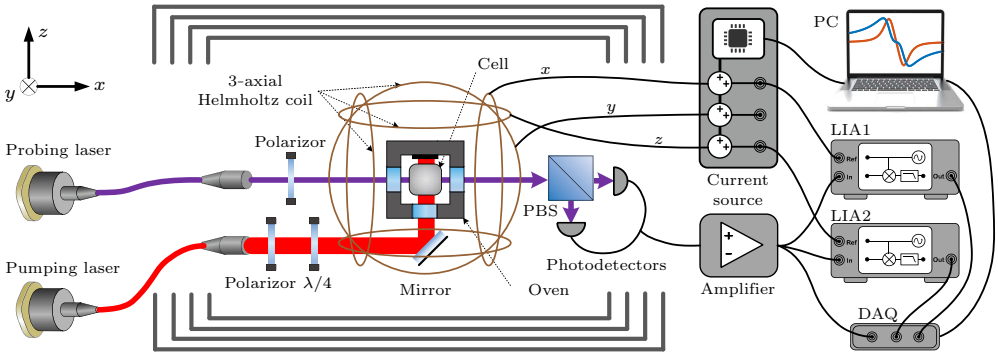


Fig. 1. Schematic of the experimental setup.

The vapor cell is placed at the center of a set of triaxial Helmholtz coils, which is used to apply the modulation fields and to control the bias fields. The coil is driven by three home-made low noise current sources, whose outputs can be controlled by a microcontroller and an external analog signal simultaneously. The two inputs are summed inside the current source. The microcontroller can scan the bias field or lock the magnetic field to zero when a proportional-integral-derivative (PID) controller algorithm is applied. The analog input can be connected to an external modulation source. Here the analog inputs of the current sources driving the coils in $\hat{x}$ and $\hat{z}$ axes are connected to the reference outputs of two lock-in-amplifiers (LIA, Stanford Research Systems, SR860). The inputs of the two lock-in-amplifiers are connected to the output of the balanced photodetector. Finally, the outputs of the two lock-in-amplifiers and the balanced photodetector are all recorded by a data acquisition (DAQ) board.

3. Theory

3.1. Vector field demodulation method given by quasi-steady-state solution

The evolution of the atomic spin polarization $\boldsymbol{P}$ in a magnetic field $\boldsymbol{B}$ can be described by the Bloch equation

$$\frac{\mathrm{d}\boldsymbol{P}}{\mathrm{d}t} = \gamma \boldsymbol{B} \times \boldsymbol{P} + R_{\mathrm{p}}\left(\frac{1}{2}s\hat{z} - \boldsymbol{P}\right) - R_{\mathrm{rel}}\boldsymbol{P}, \tag{1}$$

where γ denotes gyromagnetic ratio of potassium, R_{p} indicates pumping rate, s indicates the optical-pumping vector along $\hat{z}$ axis, and R_{rel} is total relaxation determined by spin exchange collision, spin destruction, and so forth. In the case of a slowly

varying magnetic field $\boldsymbol{B}$, by setting $\mathrm{d}\boldsymbol{P}/\mathrm{d}t = 0$, we can obtain the steady-state solution of the $\hat{x}$-component P_x as

$$P_x = P_0 \frac{\Delta\omega/\gamma B_y + B_x B_z}{\Delta\omega^2/\gamma^2 + B_x^2 + B_y^2 + B_z^2}, \tag{2}$$

where $\Delta\omega = R_\mathrm{p} + R_\mathrm{rel}$ is the magnetic resonance linewidth of the system, P_0 is the equilibrium spin polarization in the absence of any magnetic field given by $P_0 = sR_\mathrm{p}/(2\Delta\omega)$.

According to the theory in Refs. [16,21], modulation fields $B_x = B_{x0} + B_x^\mathrm{m}\cos(\omega_x t)$ and $B_z = B_{z0} + B_z^\mathrm{m}\cos(\omega_z t)$ are introduced along the x and y axes, respectively. Here, B_{x0} and B_{z0} are the bias components in the $\hat{x}$ and $\hat{z}$ axes, B_x^m and B_z^m are the modulation amplitudes. Then, Eq. (2) is expanded as

$$\begin{aligned} P_x =& P_0 \frac{\Delta\omega/\gamma B_y + B_{x0}B_{z0} + B_{x0}B_z^\mathrm{m}\cos(\omega_z t) + B_{z0}B_x^\mathrm{m}\cos(\omega_x t)}{\Delta\omega^2/\gamma^2 + B_x^2 + B_y^2 + B_z^2} \\ &+ P_0 \frac{B_x^\mathrm{m}B_z^\mathrm{m}\cos[(\omega_x+\omega_z)t] + B_x^\mathrm{m}B_z^\mathrm{m}\cos[(\omega_x-\omega_z)t]}{\Delta\omega^2/\gamma^2 + B_x^2 + B_y^2 + B_z^2}. \end{aligned} \tag{3}$$

In the case that $|\boldsymbol{B}| \ll \Delta\omega/\gamma$ and the components of frequencies $(\omega_x+\omega_z)$ and $(\omega_x-\omega_z)$ are ignored, Eq. (3) can be simplified to

$$\begin{aligned} P_x =& \frac{P_0\gamma^2}{\Delta\omega^2}[\Delta\omega/\gamma B_y + B_{x0}B_{z0} + B_{x0}B_z^\mathrm{m}\cos(\omega_z t) \\ &+ B_{z0}B_x^\mathrm{m}\cos(\omega_x t)]. \end{aligned} \tag{4}$$

Thus B_{x0} and B_{z0} can be demodulated from the components of frequencies ω_z and ω_x in P_x, respectively. If the magnetic field canceling feedback loops are established, B_{x0} and B_{z0} can be treated as zero and B_y can be obtained from DC component.

Equation (3) indicates that the response of demodulated signals to B_{x0} and B_{z0} are both given by a dispersive curve. The sensitivities of B_{x0} and B_{z0} depend on the slope at the center of the dispersive curve. The amplitude of the dispersive curve is independent of the modulation frequencies according to Eq. (3). In order to improve the response speed of the magnetic field cancelation feedback and to suppress the power line frequency noise and its harmonics, the modulation frequencies should be as high as possible. However, the actual response of the system will deviate from the quasi-steady-state solution as the modulation frequencies increase. The form of the response and its relationship with modulation frequencies should be discussed further. To simplify the problem, we discuss the responses of the two modulations separately and only consider the response at the fundamental frequency.

3.2. Response to B_{z0} given by frequency-dependence solution

Considering the condition that a bias magnetic field along $\hat{z}$ axis $\boldsymbol{B}_{z0} = \omega_{z0}/\gamma\hat{z}$ and bias magnetic fields of other axes is zeroed. The transverse components of the spin and transverse magnetic field can be written in the complex form as

$$\tilde{P}_{xy} = P_x + \mathrm{i}P_y$$

$$\tilde{B}_{xy} = B_x + \mathrm{i}B_y. \tag{5}$$

The evolution of the spin projection in x–y plane can be given by the transverse Bloch equation

$$\frac{\mathrm{d}\tilde{P}_{xy}}{\mathrm{d}t} = \mathrm{i}\gamma\left(\frac{\omega_{z0}}{\gamma}\tilde{P}_{xy} - P_0\tilde{B}_{xy}\right) - \Delta\omega\tilde{P}_{xy}. \tag{6}$$

With a modulation field along $\hat{x}$ axis $\boldsymbol{B}_x^\mathrm{m} = B_x^\mathrm{m}\cos(\omega_x t)\hat{x}$, which can be decomposed into $\tilde{B}_x^\mathrm{m} = \mathrm{i}B_x^\mathrm{m}(\mathrm{e}^{\mathrm{i}\omega_x t} + \mathrm{e}^{-\mathrm{i}\omega_x t})/2$, the response to the field $\tilde{B}_x^\mathrm{m}$ is given by the solution to Eq. (6).

The probe beam measures the spin component $P_x = \mathrm{Re}[\tilde{P}_{xy}]$, given by

$$P_x = A_{mx}^\mathrm{i}\cos(\omega_x t) + A_{mx}^\mathrm{o}\sin(\omega_x t), \tag{7}$$

with

$$\begin{aligned} &A_{mx}^\mathrm{i}(\omega_x, \omega_{z0}) \\ &= \frac{1}{2}P_0\gamma B_x^\mathrm{m}\left[\frac{(\omega_{z0}-\omega_x)}{\Delta\omega^2 + (\omega_{z0}-\omega_x)^2} + \frac{\omega_{z0}+\omega_x}{\Delta\omega^2 + (\omega_{z0}+\omega_x)^2}\right], \\ &A_{mx}^\mathrm{o}(\omega_x, \omega_{z0}) \\ &= \frac{1}{2}P_0\gamma B_x^\mathrm{m}\left[\frac{\Delta\omega}{\Delta\omega^2 + (\omega_{z0}-\omega_x)^2} - \frac{\Delta\omega}{\Delta\omega^2 + (\omega_{z0}+\omega_x)^2}\right]. \end{aligned} \tag{8}$$

From Eq. (8), the responses of in-phase component A_{mx}^i or out-of-phase component A_{mx}^o to magnetic fields $B_{z0} = \omega_{z0}/\gamma$ is given by two overlapping dispersive or Lorentzian curves centered at $+\omega_x/\gamma$ and $-\omega_x/\gamma$, respectively. The numerical calculation results of Eq. (8) are given in Fig. 2.

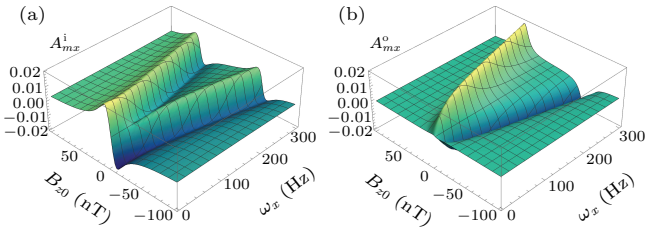


Fig. 2. The numerically analyzed result of Eq. (8) with $\Delta\omega = 50$ Hz in the ranges of $B_{z0} \in [-100, 100]$ nT and $\omega_x \in [1, 300]$ Hz. (a) The in-phase component A_{mx}^i demodulated from P_x as a function of ω_x and B_{z0}. (b) The out-of-phase component A_{mx}^o demodulated from P_x as a function of ω_x and B_{z0}.

3.3. The response to B_{x0} given by frequency-dependence solution

Considering that a bias magnetic field along $\hat{x}$ axis $\boldsymbol{B}_{x0} = \omega_{x0}/\gamma\hat{x}$ and bias magnetic field of $\hat{y}$ and $\hat{z}$ axis are zeroed, the spin polarization precesses around the $\hat{x}$ axis. We can give the transverse Bloch equation in y–z plane as follows:

$$\frac{\mathrm{d}\tilde{P}_{yz}}{\mathrm{d}t} = (\mathrm{i}\omega_{x0} - \Delta\omega)\tilde{P}_{yz} + \mathrm{i}\frac{1}{2}sR_\mathrm{p}, \tag{9}$$

where $\tilde{P}_{yz} = P_y + \mathrm{i}P_z$. From Eq. (9), $\tilde{P}_{yz}$ can be derived as follows:

$$\tilde{P}_{yz} = C\mathrm{e}^{-\Delta\omega t}\cos(\omega_{x0}t) - \frac{sR_\mathrm{p}\omega_{x0}}{2(\omega_0^2 + \Delta\omega^2)}$$

$$+\mathrm{i}\left[C\mathrm{e}^{-\Delta\omega t}\sin(\omega_{x0}t)+\frac{sR_{\mathrm{p}}\Delta\omega}{2(\omega_{x0}^2+\Delta\omega^2)}\right]. \tag{10}$$

C is a constant. P_y is given by the real part of $\tilde{P}_{yz}$, ignoring the first item in Eq. (10) which will decay to zero,

$$P_y=\frac{sR_{\mathrm{p}}\omega_{x0}}{2(\omega_{x0}^2+\Delta\omega^2)}. \tag{11}$$

When a modulation field along $\hat{z}$ axis $\boldsymbol{B}_z=B_z^{\mathrm{m}}\cos(\omega_z t)\hat{z}$ is applied, bringing P_y and B_z^{m} into the $\hat{x}$-direction Bloch equation yields

$$\frac{\mathrm{d}P_x}{\mathrm{d}t}=-B_zP_y\gamma-\Delta\omega P_x, \tag{12}$$

P_x can be derived as follows:

$$P_x=A_{mz}^{\mathrm{i}}\cos(\omega_z t)+A_{mz}^{\mathrm{o}}\sin(\omega_z t), \tag{13}$$

with

$$\begin{aligned}A_{mz}^{\mathrm{i}}(\omega_z,\omega_{x0})&=\gamma B_z^{\mathrm{m}}P_0\frac{\omega_{x0}}{(\omega_{x0}^2+\Delta\omega^2)}\frac{\Delta\omega^2}{(\Delta\omega^2+\omega_z^2)},\\ A_{mz}^{\mathrm{o}}(\omega_z,\omega_{x0})&=\gamma B_z^{\mathrm{m}}P_0\frac{\omega_{x0}}{(\omega_{x0}^2+\Delta\omega^2)}\frac{\omega_z\Delta\omega}{(\Delta\omega^2+\omega_z^2)}.\end{aligned} \tag{14}$$

From Eq. (14), the responses of in-phase component A_{mz}^{i} or out-of-phase component A_{mz}^{o} to $B_{x0}=\omega_{x0}/\gamma$ are given by a dispersion curve centered at zero, whose amplitude depends on the modulation frequency ω_z in a form of Lorentzian or dispersive shape, as shown in Fig. 3.

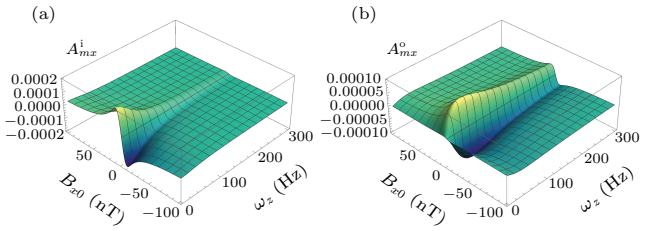


Fig. 3. The numerically analyzed result of Eq. (14) with $\Delta\omega=50$ Hz in the ranges of $B_{x0}\in[-100,100]$ nT and $\omega_z\in[1,300]$ Hz. (a) The in-phase component A_{mz}^{i} demodulated from P_x as a function of ω_z and B_{x0}. (b) The out-of-phase component A_{mz}^{o} demodulated from P_x as a function of ω_z and B_{x0}.

4. Result and discussion

In order to measure the response of the magnetometer more precisely and offer the condition of the SERF regime, the residual magnetic field in the shielding cylinder was canceled further by the triaxial compensation coils. Modulation fields are applied in $\hat{x}$ and $\hat{z}$ axes in turn according to Eq. (4). The modulation frequency is set to 3 Hz to ensure the validity of the quasi-steady-state solution. The applied compensation fields are adjusted by detecting the components of DC or 3 Hz. The specific process is as follows: First, the modulation field is applied on $\hat{x}$ axis, and the bias field on $\hat{z}$ axis is adjusted to minimize the 3 Hz component in the output signal. Likewise, the bias field on $\hat{x}$ axis is adjusted to minimize the 3 Hz component when the modulation field is applied on $\hat{z}$ axis. Then the bias field on $\hat{y}$ is adjusted to zero of the DC component. In actual operation, the offset of one axis may need to be readjusted after the offset of the other axis is changed. Therefore, we repeat this process until the offsets on all three axes become stabilized. In subsequent experiments, we take this state as the zero magnetic field point.

When the magnetic field offsets of the other two axes are canceled, by setting the corresponding terms in Eq. (2) to zero, the response to the bias field on $\hat{y}$ axis B_{y0} can be given by

$$P_x=P_0\frac{\Delta\omega/\gamma B_y}{\Delta\omega^2/\gamma^2+B_y^2}. \tag{15}$$

It can be seen from Eq. (15) that the response to B_{y0} is in the form of a dispersion curve. By scanning B_{y0}, we measured this response as shown in Fig. 4. The fitting results of this response indicate that, within the gyromagnetic ratio range of 4.7–7, the magnetic resonance linewidth $\Delta\omega$ of the system is between 40 Hz and 60 Hz.

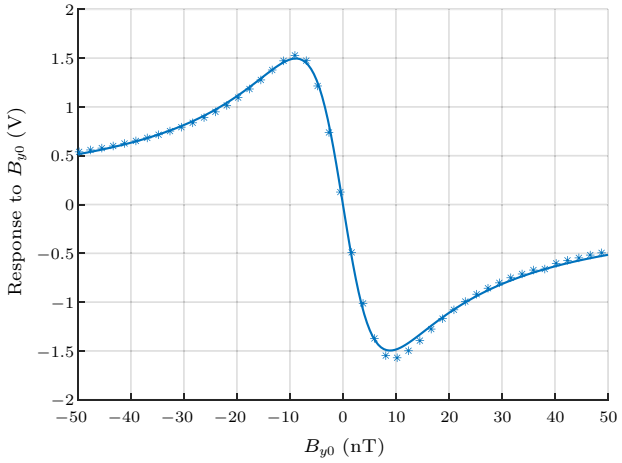


Fig. 4. The magnetometer response obtained by scanning B_{y0} and the curve of fitting by Eq. (15).

To observe the response forms of the B_{x0} and B_{z0} and their relationships to the modulation frequency, a series of modulation fields at different frequencies are applied in the $\hat{x}$ and $\hat{z}$ axes respectively, and B_{x0} or B_{z0} are swept accordingly. With 5 Hz, 60 Hz, and 600 Hz modulations on $\hat{x}$ axis, the scanning results of B_{z0} and the fitting results of Eq. (8) are shown in Figs. 5(a), 5(b), and 5(c). With 5 Hz, 40 Hz, and 600 Hz modulations on $\hat{z}$ axis, the scanning results of B_{x0} and the fitting results of Eq. (14) are shown in Figs. 5(d), 5(e), and 5(f).

We could find that the in-phase signals reach the maximum, and the out-of-phase signals will approach zero when the modulation frequencies are much lower relative to $\Delta\omega$, no matter whether it is for modulations along the $\hat{x}$ axis or the $\hat{z}$ axis. This implies that the responses converge to the quasi-steady-state solution. Under the condition that the modulation

frequencies are close to the linewidth $\Delta\omega$, the in-phase signal responding to the modulation in $\hat{x}$ axis is insensitive to B_{z0} near zero meanwhile the slope of the out-of-phase signal is maximized. The in-phase and out-of-phase signals responding to the modulation in $\hat{z}$ axis perform equal amplitude. In our experiments, the frequency with equal in-phase and out-of-phase signal amplitudes occurs at 40 Hz, which differs by about 15 Hz from the magnetic resonance linewidth measured by B_{y0} scanning. One of the reasons may be that we neglected the difference of the polarization relaxation times in the $\hat{z}$ axis direction and in x–y planes in our calculations. In the case that the modulation frequency is much larger than the linewidth $\Delta\omega$, the slope of the out-of-phase signal near the zero magnetic field is larger than the in-phase signal. However, they are both attenuated a lot in two modulations.

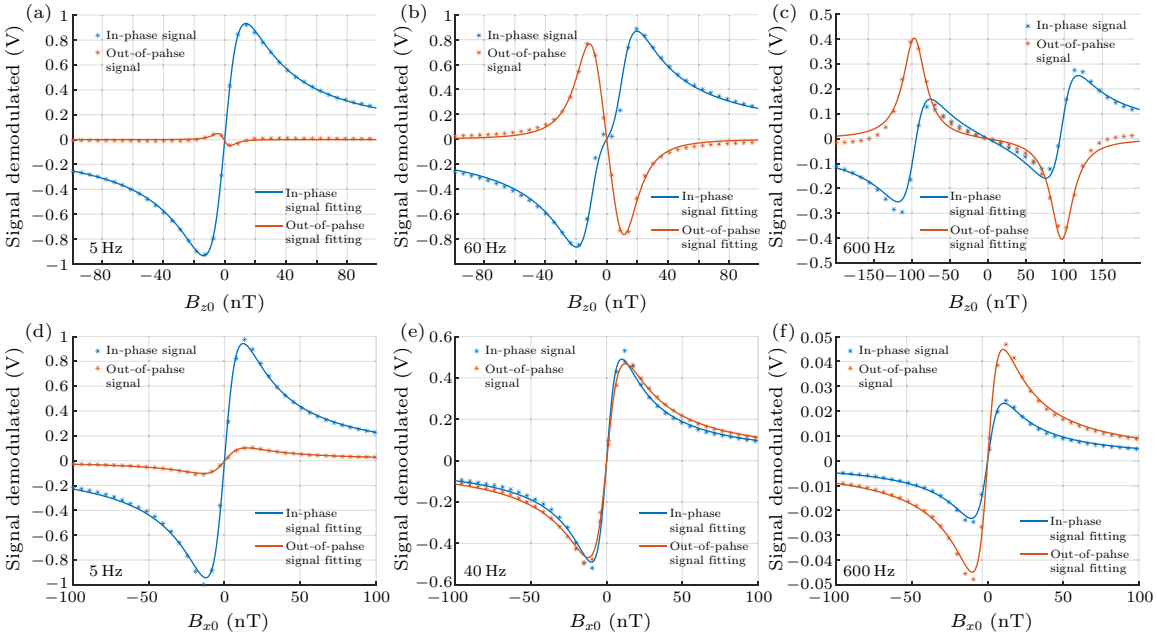


Fig. 5. The system responses to B_{z0} and B_{x0} under different modulation frequencies. (a) The response to B_{z0} with modulation field of 5 Hz in $\hat{x}$ axis. (b) The response to B_{z0} with modulation field of 60 Hz in $\hat{x}$ axis. (c) The response to B_{z0} with modulation field of 600 Hz in $\hat{x}$ axis. (d) The response to B_{x0} with modulation field of 5 Hz in $\hat{z}$ axis. (e) The response to B_{x0} with modulation field of 40 Hz in $\hat{z}$ axis. (f) The response to B_{x0} with modulation field of 600 Hz in $\hat{z}$ axis.

In addition, we further investigate the frequency response of the system to the triaxial magnetic field components. For unshielded applications, the frequency response of the magnetometer is also important because it is directly related to the bandwidth that the magnetic field feedback compensation system can achieve.

In the solutions given in Subsections 3.2 and 3.3, we only considered the fundamental frequency components of the modulation frequencies. However, for the actual signal, there are not only the harmonics of the modulation frequencies but also the sum and difference frequency components of the two modulation frequencies, which are also been indicated by Eq. (3).

To compromise between the amplitude of the signal and the bandwidth that can be achieved after demodulation, the modulation frequency in $\hat{x}$ axis is set to 150 Hz and that in $\hat{z}$ axis is set to 250 Hz, which also ensures that there will be no spurious signals caused by modulation within the frequency band of 100 Hz. The effective values of the modulation signals are all 20 nT. The time constants of the two lock-in amplifiers are both set to 3 ms and the filter slopes are set to 6 dB. The same parameters are applied for the low-pass filter which extracts the $\hat{y}$ axis signal. Another lock-in-amplifier is used to apply AC magnetic fields with an effective value of 1 nT on three axes sequentially. The fields are offered by the self-contained coils by the shielding cylinder which is composed of a solenoid and two sets of saddle coils, and are not shown in Fig. 1. The frequency of the fields is swept in the range of 1–100 Hz to test the frequency response of demodulated signal to the triaxial magnetic field components, and the results are shown in Fig. 6.

The in-phase and out-of-phase components in the frequency response of the $\hat{y}$ axis magnetic field are in the forms of Lorentzian and dispersion curves, respectively, which are given by[21]

$$F(\omega) = \frac{K\cdot\Delta\omega}{(\omega-\omega_0)^2+\Delta\omega^2}+C,$$
$$F(\omega) = \frac{K\cdot(\omega-\omega_0)}{(\omega-\omega_0)^2+\Delta\omega^2}+C, \tag{16}$$

where $F(\omega)$ is the fitted function, K is the amplitude, $\Delta\omega$ is the linewidth, ω_0 is the peak position, and C is the baseline offset.

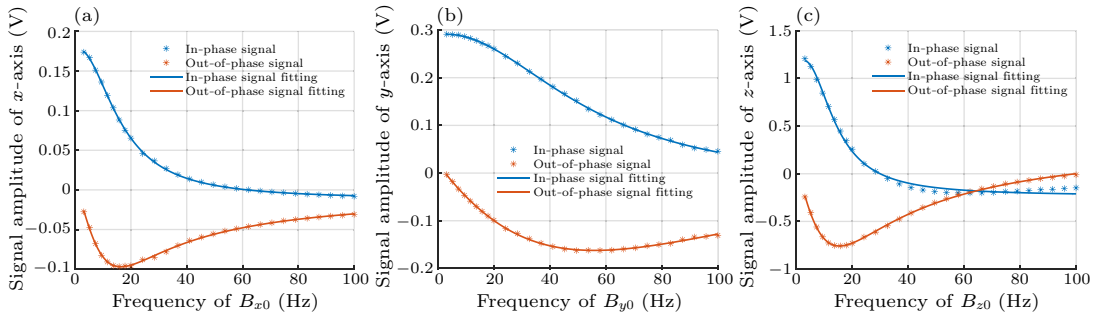


Fig. 6. The open-loop frequency response of demodulated signal to the triaxial magnetic field components. (a) The frequency response to $\hat{x}$ axis component. (b) The frequency response to $\hat{y}$ axis component. (c) The frequency response to $\hat{z}$ axis component.

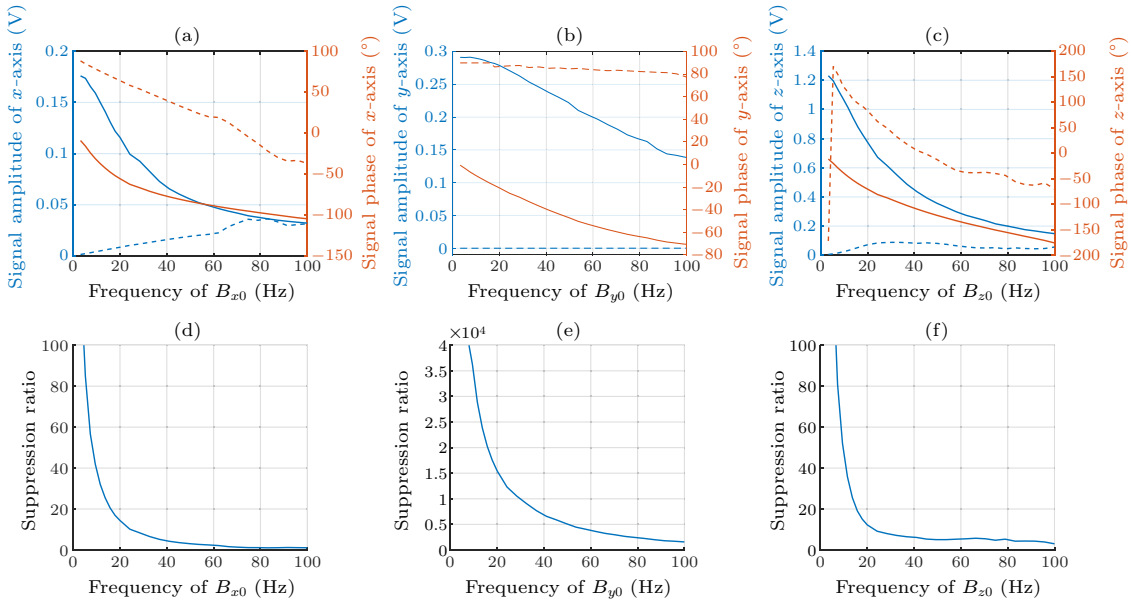


Fig. 7. The closed-loop frequency response of the amplitude and phase of the signal to the triaxial magnetic field components compared with the open-loop response. The open-loop responses are marked with solid lines, and the closed-loop responses are marked with dashed lines. Blue represents the magnitude response and red represents the phase. (a) The frequency response to $\hat{x}$ axis component. (b) The frequency response to $\hat{y}$ axis component. (c) The frequency response to $\hat{z}$ axis component. (d) The inhibition ratio to $\hat{x}$ axis component. (e) The inhibition ratio to $\hat{y}$ axis component. (f) The inhibition ratio to $\hat{z}$ axis component.

Interestingly, for the demodulated signals of $\hat{x}$ and $\hat{z}$ axes, the in-phase and out-of-phase components in their frequency responses can also be well fitted by Lorentzian and dispersive curves. It should be noted that in this test, the signal of $\hat{x}$ axis which is demodulated from the modulation in $\hat{z}$ axis is given by the out-of-phase component, because at the set modulation frequency the amplitude of the out-of-phase signal is much larger than that of the in-phase signal. The signal of $\hat{z}$ axis which is demodulated from the modulation in $\hat{x}$ axis is given by the in-phase component because of its larger amplitude. Of course, the signal amplitude can be maximized by optimizing the demodulation phase. Herein, we tend to show this result which is in good agreement with the Lorentzian and dispersion curves in the experiments. The signal amplitude improvement brought from the phase optimizing will not be too much. This suggests that a uniform control algorithm can be employed for providing feedback control to magnetic fields in all three directions, requiring parameter adjustments exclusively.

Based on the frequency response results given above, we design the three-axis magnetic field feedback compensation. The PID control algorithm is implemented by the microcontroller, and the three-way output signals of the system are read by the three analog-to-digital converters (ADCs) directly controlled by the microcontroller, due to the real-time requirements of the feedback system. The test magnetic fields are still provided by the shielding cylinder's own coils and are still swept in the range of 1–100 Hz. After the closed-loop compensation is established, the frequency response of the system is measured again, as shown in Fig. 7. For comparison, the results without feedback compensation are also shown again in Fig. 7 in the form of bode plot (in comparison with the in-phase and out-of-phase signals in Fig. 6, here the Bode plot system is used to compare the system responses). Additionally, the proportional relationship between the two response curves is utilized to showcase the attenuation ratio. Utilizing the mentioned modulation frequencies and operating within the vicinity of the DC frequency range, a remarkably pronounced suppression effect on the magnetic field becomes evi-

dent. Notably, the suppression ratios for the ambient magnetic fields exceed 10 times within the frequency band below 20 Hz along all three axes. The ratios are not less than 3 and 5 times at 50 Hz in $\hat{x}$ and $\hat{z}$ axes. The capability of the suppression to power line noise shows the potential of the system to operate in a completely unshielded environment.

5. Conclusions

In this work, a model describing the response of the three-axis SERF magnetometer under high frequency modulations is presented and verified experimentally, which can serve as a reference for modulation frequency selection. We observe a magnetic resonance linewidth of approximately $\Delta\omega \approx 55$ Hz. Across the specified modulation frequency, the suppression ratios for all three axes relative to the ambient magnetic field exceed 10 within the frequency range below 20 Hz. At 50 Hz, the suppression ratios along the x and z axes are at least 3 and 5 times, respectively. The magnetic field canceling experimental result shows an ability to suppress power frequency noise of the system, which reflects its potential to operate in a geomagnetic field environment without heavy aluminum shielding.

Acknowledgment

Project supported by the National Natural Science Foundation of China (Grant No. 42074216).

References

[1] Jiang M, Su H, Garcon A, Peng X and Budker D 2021 *Nat. Phys.* **17** 1402
[2] Bloch I M , Ronen G, Shaham R, Katz O, Volansky T and Katz O 2022 *Sci. Adv.* **8** eabl8919
[3] Afach S, Buchler B C, Budker D, *et al.* 2021 *Nat. Phys.* **17** 1396
[4] Ledbetter M, Savukov I, Budker D, Shah V, Knappe S, Kitching J, Michalak D, Xu S and Pines A 2008 *Proc. Natl. Acad. Sci. USA* **105** 2286
[5] Boto E, Holmes N, Leggett J, *et al.* 2018 *Nature* **555** 657
[6] Robinson J T, Pohlmeyer E, Gather M C, Kemere C, Kitching J E, Malliaras G G, Marblestone A, Shepard K L, Stieglitz T and Xie C 2019 *IEEE Sensors J.* **19** 10163
[7] Dang H, Maloof A C and Romalis M V 2010 *Appl. Phys. Lett.* **97** 151110
[8] Budker D and Romalis M V 2007 *Nat. Phys.* **3** 227
[9] Wyllie R, Kauer M, Smetana G S, Wakai R T and Walker T G 2012 *Phys. Medicine Biol.* **57** 2619
[10] Fang J, Li R, Duan L, Chen Y and Quan W 2015 *Rev. Sci. Instrum.* **86** 073116
[11] Wang M L, Wang M B, Zhang G Y and Zhao K F 2016 *Chin. Phys. B* **25** 060701
[12] Johnson C, Schwindt P D D and Weisend M 2010 *Appl. Phys. Lett.* **97** 243703
[13] Li Y, Wang Z, Jin S, Yuan J and Luo H 2017 *Sci. Rep.* **7** 43066
[14] Li Z, Wakai R T and Walker T G 2006 *Appl. Phys. Lett.* **89** 134105
[15] Shah V and Romalis M V 2009 *Phys. Rev. A* **80** 013416
[16] Seltzer S and Romalis M V 2004 *Appl. Phys. Lett.* **85** 4804
[17] Li Z, Wakai R T and Walker T G 2006 *Appl. Phys. Lett.* **89** 134105
[18] Patton B, Zhivun E, Hovde D and Budker D 2014 *Phys. Rev. Lett.* **113** 013001
[19] Huang H, Dong H, Hu X, Chen L and Gao Y 2015 *Appl. Phys. Lett.* **107** 182403
[20] Huang H, Dong H, Chen L and Gao Y 2016 *Appl. Phys. Lett.* **109** 062404
[21] Seltzer S J 2008 *Developments in Alkali-Metal Atomic Magnetometry* (Ph.D. Dissertation) (Princeton University)